applied sciences

MDPI

Article

Flexural Performance of Composite-Reinforced Prestressed Concrete Hollow Square Piles: Experimental and Numerical Analysis

Hongli Xie and Zhijun Zhou *

School of Highway, Chang'an University, Xi'an 710061, China; 2022021008@chd.edu.cn
* Correspondence: zhouzhijun@chd.edu.cn

Abstract

To investigate the stress evolution, deformation behavior, and failure characteristics of composite-reinforced prestressed concrete hollow square piles (PHSC piles) under bending, a four-point bending test was conducted on a full-scale PHSC500 (340) hollow square pile specimen with a length of 7000 mm, a square section of 500 mm × 500 mm, and a hollow core diameter of 340 mm. The test was used to obtain load–deflection curves, crack propagation patterns, deformation responses, sectional strain distributions, and failure modes. In addition, an ABAQUS finite element model was established to compare the bearing capacity, stiffness degradation, and ductility of different pile types with varying prestressed and non-prestressed reinforcement ratios. The results show that vertical cracks changed their propagation direction at the edge of the tensile zone in the flexural–shear region of the PHSC piles and developed into a critical diagonal crack with a width of 1.7 mm. The specimen ultimately exhibited a shear–compression failure mode. During the failure stage, the midspan deflection increased rapidly as the load rose from 710 to 740 kN, with the deflection increasing from 24.88 to 32.00 mm. The load–midspan deflection curve obtained from the finite element analysis was generally consistent with the experimental results. Moreover, the predicted damage concentration zones corresponded well to the experimentally observed crack locations, indicating that the model can be used to analyze relative variations under different parameter conditions. The combination of prestressed and non-prestressed reinforcement improved the flexural capacity and ductility of the PHSC piles. However, ductility did not increase monotonically with the prestressed reinforcement ratio. These findings provide a reference for evaluating the flexural performance of PHSC hollow square piles and optimizing their reinforcement parameters.

Keywords: highway engineering; PHSC pile; flexural performance; cracking moment; finite element analysis

Check for updates

Academic Editor: Doo Yeol Yoo

Received: 24 May 2026
Revised: 27 June 2026
Accepted: 29 June 2026
Published: 30 June 2026

Copyright: © 2026 by the authors. Licensee MDPI, Basel, Switzerland. This article is an open access article distributed under the terms and conditions of the Creative Commons Attribution (CC BY) license.

1. Introduction

As foundation pit engineering technology continues to advance, prestressed concrete pipe piles are now widely employed in foundation pit support systems to ensure construction safety [1–3]. However, the inadequate horizontal bearing capacity and subpar seismic performance of this pile type significantly impede its further development [4,5]. Monitoring data indicate that, under horizontal loads, prestressed concrete pipe piles frequently exhibit quality defects, including cracking, tilting, and even fracture, due to insufficient flexural bearing capacity [6]. Their cracking bending moment is near the ultimate bending moment, substantially elevating the risk of engineering accidents. Ordinary precast concrete

square piles offer high flexural bearing capacity and good deformation ductility; however, they suffer from drawbacks such as a generally low concrete strength grade, inadequate structural crack resistance, and a lengthy production cycle. Furthermore, cracks are likely to develop during logistics transportation, on-site hoisting, and temporary stacking, potentially leading to fracture in severe cases. This significantly limits the applicability and promotional value of this pile type in engineering construction [7,8].

To overcome the limitations of traditional precast concrete square piles in engineering applications, a novel composite-reinforced prestressed concrete square pile is proposed, leveraging the distinct advantages of prestressed concrete pipe piles and prestressed concrete precast square piles [9–13]. This pile type substantially increases the crack resistance of concrete square piles through prestressing [14,15] and incorporates ordinary threaded steel bars to enhance its flexural capacity [16–19]. Composite-reinforced prestressed concrete solid square piles not only feature a large cross-sectional area but also exhibit significantly enhanced horizontal bearing capacity and ductility compared to prestressed concrete pipe piles and traditional precast concrete square piles [20]. Additionally, composite-reinforced prestressed concrete hollow square piles offer greater material economy compared to solid square piles [21]. When high flexural performance is required, ordinary concrete can be poured into the cavity to further augment its flexural capacity and enhance its flexibility.

Numerous scholars have conducted extensive research on both solid and hollow concrete square piles [22–26]; however, research on the composite reinforcement of hollow concrete square piles remains relatively scarce [27]. Sun et al. [28] investigated the impact of prestressed tension control stress, anchoring methods, and the hot-rolled steel reinforcement ratio of PC bars on the seismic performance of snap-on mechanical connection prestressed concrete solid square pile cap joints. They also proposed measures to enhance the stress performance of these piles and their pile cap joints. Su and Wu [29] examined the bending performance of reinforced concrete beams reinforced with glass fiber-reinforced polymer (GFRP) bars and coated with three-sided ultra-high-performance concrete (UHPC) layers, using both experimental and numerical simulation methods. They suggested that applying UHPC layers can effectively limit crack width development on the beam surface. Xu et al. [30] compared the crack resistance, flexural capacity, deformation ductility, and failure characteristics of prestressed and non-prestressed precast square piles. They discovered that prestressing significantly enhances the crack resistance of square piles. Relevant studies have also shown that a rational combination of prestressing steel bars and non-prestressed reinforcement can improve the flexural capacity and deformation capacity of concrete members [31,32]. However, most existing studies have focused on PHC pipe piles, composite-reinforced solid square piles, or conventional prestressed concrete members. Research on composite-reinforced prestressed concrete hollow square piles, namely PHSC hollow square piles, under flexural loading remains limited [27]. In this study, the term "composite-reinforced" refers specifically to the reinforcement system of PHSC hollow square piles, in which prestressing steel bars and non-prestressed deformed steel bars are combined within the same hollow square section. It does not denote a material-level composite system.

Compared with solid square piles, PHSC hollow square piles have a hollow section. The reduced section may affect the stress distribution in the tensile and compressive zones, the crack propagation path, and the final failure mode. Compared with conventional PHC pipe piles, PHSC hollow square piles contain both prestressing steel bars and non-prestressed reinforcement. These two reinforcement systems contribute differently to crack resistance, bearing capacity, and deformation capacity before and after cracking. Therefore, findings obtained from PHC pipe piles, solid square piles, or conventional prestressed concrete members cannot fully explain the crack development, strain evolution, and ultimate

failure characteristics of PHSC hollow square piles under flexural loading. In particular, none of the cited studies is fully consistent with the present work in terms of member type, specimen scale, loading method, and research scope. Systematic investigations on full-scale PHSC500 (340) hollow square piles (Jianhua Building Materials (Shaanxi) Co., Ltd., Xianyang, Shaanxi, China) under four-point bending, including crack deflection, strain evolution, stiffness degradation, shear–compression failure, and the effect of reinforcement ratio, remain limited. Based on this background, a full-scale PHSC500 (340) hollow square pile specimen was tested in this study to examine its ultimate load-bearing capacity, deformation profile, crack distribution, and strain development under flexural loading. ABAQUS finite element models were further established to evaluate the effects of pile type and reinforcement-ratio combinations. The results provide a theoretical and practical basis for evaluating the flexural performance of PHSC piles and optimizing their reinforcement parameters in engineering applications.

2. Experimental Overview

2.1. Test Piece Design

This study focuses on the HZM-C07 contract section of the Fuzhou Meizhou Expressway (Figure 1), where composite-reinforced prestressed concrete hollow square piles are employed for roadbed slope reinforcement. In actual roadbed slope reinforcement projects, PHSC hollow square piles are mainly subjected to lateral earth pressure and slope thrust, which generate bending moments and shear forces along the pile height. To investigate the key flexural behavior of field piles, a full-scale representative specimen with the same geometric dimensions and reinforcement layout as the engineering pile was used in the laboratory flexural test. Although the test could not fully reproduce the complex stress environment in the field, it captured the flexural response, crack development, and failure characteristics of PHSC piles under controlled loading conditions. The pile cross-section forms a 0.5 m × 0.5 m square with a hollow core measuring 0.34 m in diameter. The prestressing tendons consist of $12A^D12.6$, with a total applied prestressing force of 1296 kN. The non-prestressed reinforcement comprises HRB400 grade rebar (6C18), while stirrups are fabricated from Grade A cold-drawn low-carbon steel wire with $A^b5@45/80$.

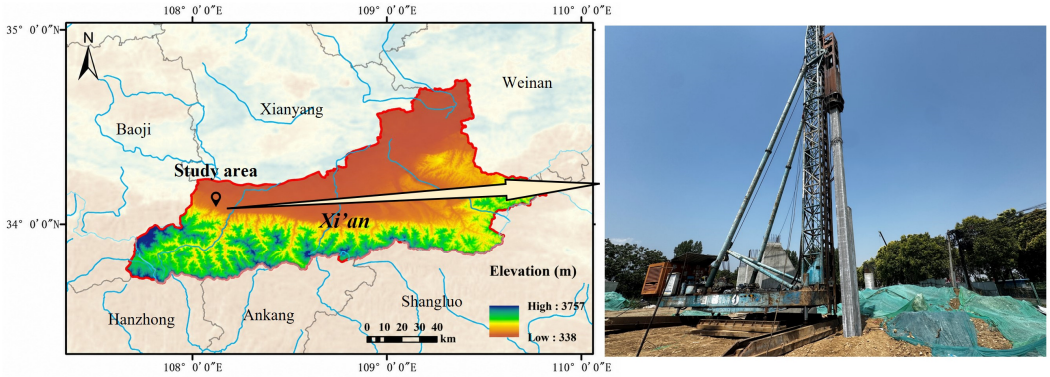


Figure 1. Field Application of the PHSC Hollow Square Pile.

According to the material property tests, the measured cube compressive strengths of concrete were 87.7, 93.8, and 80.7 MPa. The mean value was 87.40 MPa, with a standard deviation of 6.55 MPa and a coefficient of variation of 7.50%. The corresponding axial compressive strength, f_c, and tensile strength, f_t, were calculated as 54.87 and 4.49 MPa, respectively. For the HRB400 deformed steel bars, the measured yield strengths were 445 and 450 MPa. The mean value was 447.50 MPa, with a standard deviation of 3.54 MPa and a coefficient of variation of 0.79%. For the prestressing steel bars, the measured tensile

strengths were 1510, 1525, and 1520 MPa. The mean value was 1518.33 MPa, with a standard deviation of 7.64 MPa and a coefficient of variation of 0.50%. The standard tensile strength of the stirrups, f_{stk}, was taken as 550 MPa according to the relevant specification [33].

A hollow square pile was selected to investigate the flexural performance of PHSC piles. The specimen had a length L of 7 m, a side length B of 500 mm, and an inner diameter D of 340 mm. The prestressing steel bars were arranged in a square pattern with an arrangement side length B_p of 417.4 mm. The geometric dimensions and reinforcement details were consistent with those of the field pile, as shown in Figure 2 and Table 1, and the concrete cover thickness was 35 mm. The specimen was designed based on the PHSC anti-slide piles used in an actual engineering project and can therefore reasonably represent the pile type investigated in this study. Considering the large size of full-scale PHSC pile specimens and the high costs associated with fabrication and loading, a representative specimen was used for the flexural failure test. Based on the experimental results, a finite element model was further developed to analyze the effects of different pile types and reinforcement-ratio combinations on flexural performance.

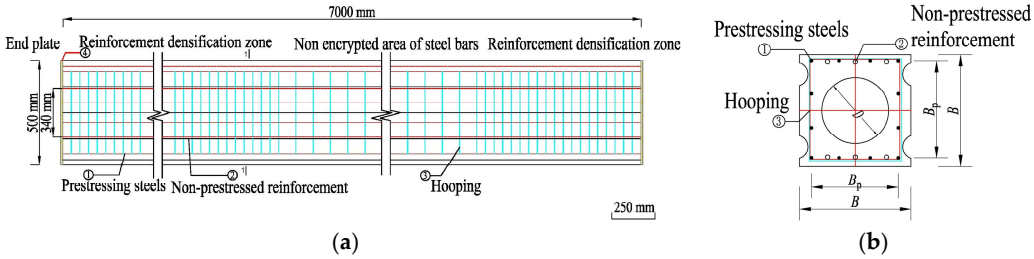


Figure 2. Schematic diagram of reinforcement for hollow square piles: (**a**) Reinforcement diagram of retaining pile structure; (**b**) 1-1 section.

Table 1. Reinforcement configuration of the hollow square pile specimen.

Specimen Number	Main Reinforcement	Prestressing Ratio (%)	Non-Prestressed Reinforcement Ratio (%)	Total Reinforcement Ratio (%)	Stirrup
PHSC500 (340)	$12A^D12.6 + 6C18$	0.94	0.96	1.9	$A^b5@45/80$

2.2. Experimental Apparatus and Loading Method

The flexural performance test of the PHSC pile was conducted in accordance with the national standards [34,35]. The test setup is shown in Figure 3. The load was applied using a 500-t synchronized hydraulic jack, and the reaction was provided by a portal reaction frame. The loading level was monitored in real time using load sensors. The specimen had a total length of 7000 mm. The distance from each end of the specimen to the center of the corresponding support was 1400 mm, giving a support span of 4200 mm. The two loading points were arranged symmetrically about the midspan, with each loading point located 500 mm from the midspan. Thus, the distance between the two loading points was 1000 mm. The distance from each loading point to the center of the adjacent support was 1600 mm, corresponding to a shear span of 1600 mm. The load was applied through a distribution beam with a length of 1500 mm. A monotonic stepwise loading protocol was adopted. After each target load level was reached, the load was maintained for at least 3 min. Once the readings were essentially stable, the load, deflection, strain, and crack width were recorded. Loading was then continued until the specimen reached its ultimate state. Displacement transducers No. 1 and No. 2 were used to measure the displacement of the pile at the supports. Displacement transducers No. 3, No. 4, and No. 5 were installed

below the loading points and at the midspan to measure the deflection. The displacement data were collected using an RSM-JC5(C) static load testing system.

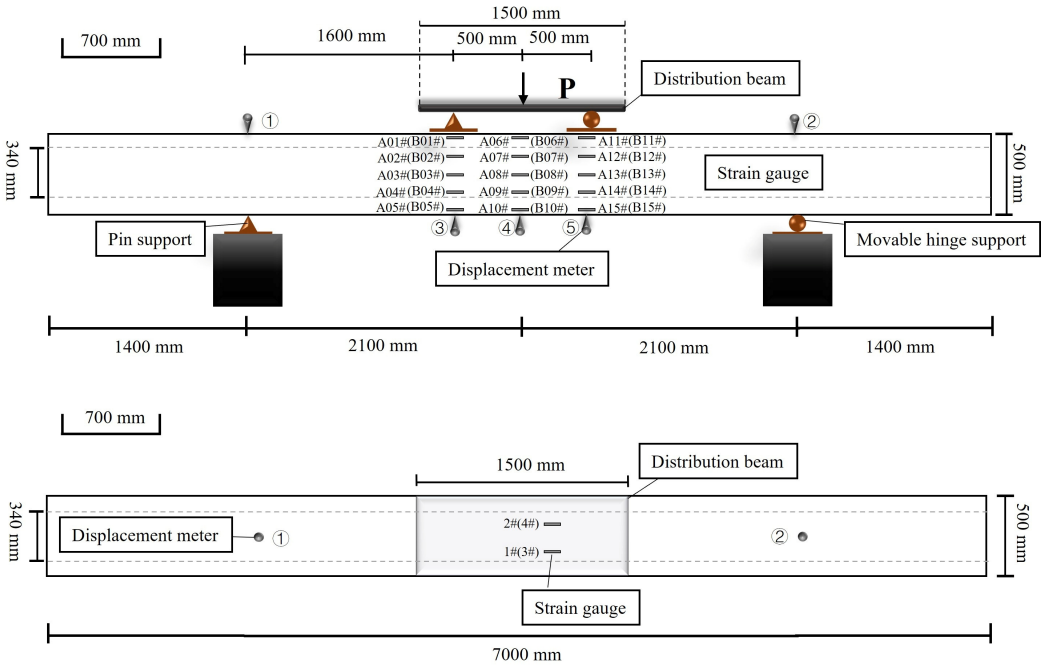


Figure 3. Experimental loading device and measurement point layout.

Five strain gauges were uniformly arranged along both the midspan section and the loading-point sections. The spacing between adjacent strain gauges was 112.5 mm. The upper and lower concrete strain gauges were placed 25 mm from the specimen edges. In addition, two strain gauges were installed on both the top and bottom surfaces at the midspan, with a spacing of 100 mm. Strain data were collected using a DH3818Y static strain testing instrument manufactured by Jiangsu Donghua Testing Technology Co., Ltd. (Jingjiang, China). The strain gauges on the back side of the PHSC pile were arranged in the same manner as those on the front side. The bending moment at the midspan section of the specimen, M_t, was calculated using Equation (1):

$$M_t = \frac{P}{4}\left(\frac{3}{5}L - 2a\right) + \frac{1}{40}WL \quad (1)$$

where: P is the load value; W is the self-weight of the hollow square pile specimen; L is the specimen length; and $2a$ is the distance between the two loading points, with a representing one-half of the loading-point spacing. According to the specification, when the outer diameter is less than 1300 mm and the length of a single pile is not greater than 15 m, a is taken as 0.5 m. When the outer diameter is greater than 800 mm and the length of a single pile is not greater than 15 m, a is taken as the outer diameter D of the pile. Equation (1) was adopted from GB/T 13476-2023 [34], which specifies the bending-moment calculation for prestressed concrete piles under four-point bending tests. It is applicable to the calculation of the midspan bending moment under simply supported conditions with two symmetrically arranged loading points. In the calculation, the total applied load is assumed to be equally distributed between the two loading points, and the self-weight of the pile is assumed to be uniformly distributed along the specimen length.

3. Experiments and Analysis

3.1. Analysis of Flexural Bearing Capacity

The moment–midspan deflection relationship shown in Figure 4 indicates that the specimen had good deformation capacity. Table 2 compares the experimental results with the values specified in the Technical Specification for Precast Concrete Sheet Pile Retaining Walls (T/CECS 582-2019) [36] and the theoretical values calculated according to the Code for Design of Concrete Structures (GB 50010-2010) [37]. As shown in Table 2, the cracking moment obtained from T/CECS 582-2019 was relatively close to the experimental result, whereas the theoretical value calculated using GB 50010-2010 differed from the test value by approximately 20.09%. Overall, the measured cracking moment of the PHSC500 (340) specimen was generally lower than the code-based predictions, whereas its ultimate flexural capacity was significantly higher than the predicted values. The theoretical calculation generally assumes an idealized section, homogeneous material properties, effective prestress transfer, and no initial defects. In practice, however, PHSC hollow square piles may exhibit material variability, initial microcracks, loading-contact deviations, stress concentration caused by the hollow section, and prestress loss. These factors may cause the local tensile stress to reach the tensile strength of concrete earlier than predicted. In addition, prestress loss and deformation incompatibility between steel and concrete may reduce the effective tensile resistance at the initial cracking stage. Therefore, the measured cracking moment was lower than the theoretical prediction.

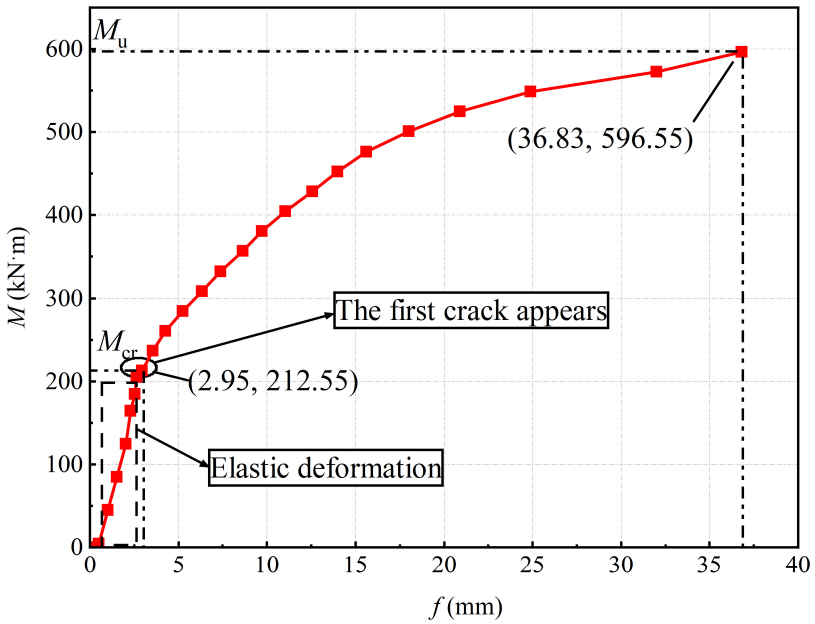


Figure 4. Bending moment–midspan deflection curve.

Table 2. Comparison of theoretical and experimental results.

Pile Type	$M_{cr,k}$ (kN·m)	$M_{cr,A}$ (kN·m)	$M_{cr,B}$ (kN·m)	$M_{cr,B}/M_{cr,k}$	$M_{cr,B}/M_{cr,A}$	M_u (kN·m)	M_{uA} (kN·m)	M_{uB} (kN·m)	M_{uB}/M_u	M_{uB}/M_{uA}
PHSC500 (340)	231	255.26	212.55	0.92	0.83	543	531.44	596.55	1.10	1.12

Note: $M_{cr,k}$ and M_u are the values taken from the "Technical Specification for Prefabricated Concrete Sheet Pile Retaining Walls" (T-CECS 582-2019); $M_{cr,A}$ and M_{uA} are the theoretical calculation values from the "Code for Design of Concrete Structures" (GB50010-2010); $M_{cr,B}$ and M_{uB} are the test results.

At the initial loading stage, the bending moment–midspan deflection response of the PHSC500 (340) specimen was approximately linear. Once the first vertical crack appeared in

the pure bending zone, the overall stiffness of the specimen began to decrease. As the load continued to increase, the cracks gradually propagated and widened, and the number of cracks also increased. Their length and width continued to grow, while the rate of deflection increase exceeded the rate of load increase, indicating the gradual accumulation of plastic deformation in the materials. Eventually, the midspan deflection increased sharply, and the member failed suddenly, accompanied by a loss of load-bearing capacity. The last loading point in Figure 4 represents the peak load recorded immediately before specimen failure. It does not indicate stiffness enhancement at the later loading stage. Instead, it reflects the rapid development of deformation as the specimen approached its ultimate state and entered the instability failure stage.

To further clarify the force-transfer mechanism of the member under flexural loading, strain gauges were installed along the pile. The maximum effective tensile strain measured during the test was approximately 2956 με. Based on the elastic modulus of C80 concrete, taken as 38,000 MPa, the corresponding nominal tensile stress was calculated to be approximately 112 MPa. This value was much higher than the measured tensile strength of concrete, which was 4.49 MPa. This indicates that the concrete in the tensile zone had already cracked at this stage. However, the tensile stress of 112 MPa does not represent the actual tensile stress carried by the concrete after cracking. Instead, it is a nominal value calculated under the assumption of an uncracked linear-elastic section. After crack formation, the continuity of the concrete in the tensile zone was reduced. The strain-gauge readings may therefore have been affected by local strain concentration near the cracks and by crack-opening deformation. Consequently, after concrete cracking, the tensile force in the tensile zone was no longer mainly carried by the concrete. It was instead transferred primarily to the prestressing steel bars and the non-prestressed reinforcement. The concrete between adjacent cracks could still carry a small amount of tensile force, but its contribution was limited. Therefore, the final failure of the specimen was not governed by tensile fracture of the concrete in the tensile zone.

Figure 5 shows the final failure mode of the PHSC500 (340) specimen and the damage condition of the reinforcement. As shown in the figure, the specimen failed when the width of the critical diagonal crack reached 1.7 mm. Concrete crushing occurred at the edge of the shear–compression zone, and the stirrups in the flexural–shear region fractured. As a result, the inclined section lost its load-bearing capacity, and the specimen ultimately exhibited a shear–compression failure mode. According to the test records, the specimen failed under a load of 740 kN. Under symmetric four-point bending, the ultimate shear force in the flexural–shear region at failure was approximately 370 kN. The shear span was approximately 1.6 m, and the section height was 0.5 m, giving a shear span-to-depth ratio of approximately 3.2. This indicates that the flexural–shear region was subjected to a considerable shear effect at the ultimate stage. Although vertical cracks first appeared in the pure bending region, the final failure was characterized by the continuous propagation of the critical diagonal crack in the flexural–shear region, concrete damage in the shear–compression zone, and stirrup fracture. These phenomena led to the loss of load-bearing capacity of the inclined section. Therefore, the failure of the specimen was mainly governed by the inclined-section capacity in the flexural–shear region, rather than by tensile fracture of the concrete in the tensile zone. According to the mechanical behavior of reinforced concrete flexural members, after concrete cracking, the tensile force in the tensile zone is mainly carried by the prestressing steel bars and non-prestressed reinforcement. The concrete between cracks carries only limited tensile force. Therefore, cracking of the concrete in the tensile zone had a relatively limited effect on the ultimate flexural capacity of the member.

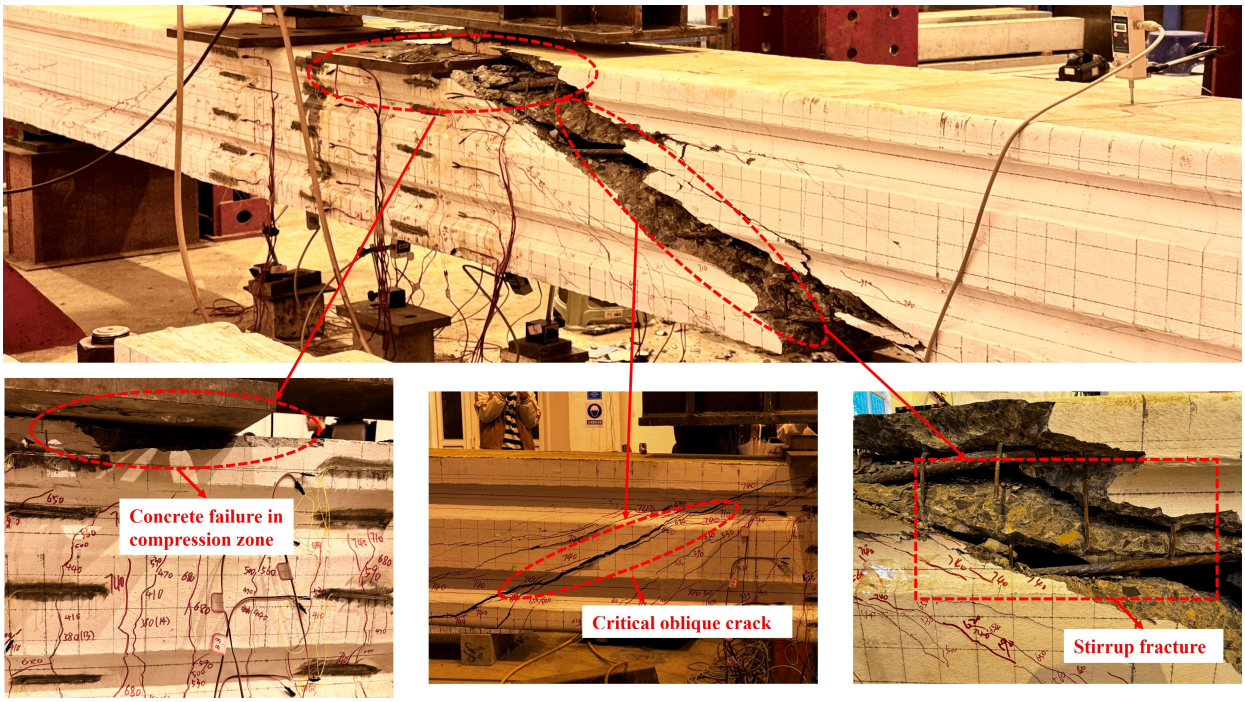


Figure 5. Test piece failure mode.

3.2. Analysis of Pile Deformation Curve

Figures 6 and 7 show the variations in the overall pile deflection and the deflection in the pure bending region of the PHSC500 (340) specimen with increasing load. Before the cracking load of 260 kN was reached, the specimen was mainly in the elastic stage. The initial tensile stress in the prestressing steel bars restrained deformation in the tensile zone, resulting in relatively small overall deflection of the pile. The deflection distribution was approximately linear, and the deformation difference within the midspan pure bending region was limited. At this stage, the overall pile deflection curve exhibited a U-shaped profile. After the load exceeded the cracking load, the pile entered the elastoplastic stage. The internal stress distribution changed markedly, and the deflection increased at a faster rate, showing a nonlinear response. When the load increased to 740 kN, the specimen failed. The midspan deflection increased sharply, and the overall pile deflection curve changed to a V-shaped profile. This behavior was caused by the combined effects of stiffness degradation due to concrete cracking and the accumulation of plastic deformation. Before cracking, the pile section remained essentially intact, and the variation in flexural stiffness along the pile length was small. As a result, the deflection at each measurement point increased gradually, and the overall deflection profile showed a U-shaped distribution. After cracking, cracks gradually developed in the midspan and flexural–shear regions. The effective flexural stiffness decreased in the crack-concentrated zones, and deformation progressively localized near the midspan. Consequently, the midspan deflection increased much faster than the deflections measured at the two sides, and the pile deflection curve gradually changed from a U-shaped profile to a V-shaped profile. At the failure stage, the midspan deflection increased rapidly. When the load increased from 710 to 740 kN, the midspan deflection increased from 24.88 to 32.00 mm, corresponding to an increase of 1.29 times. This further indicates that deformation was significantly concentrated near the midspan as the specimen approached failure.

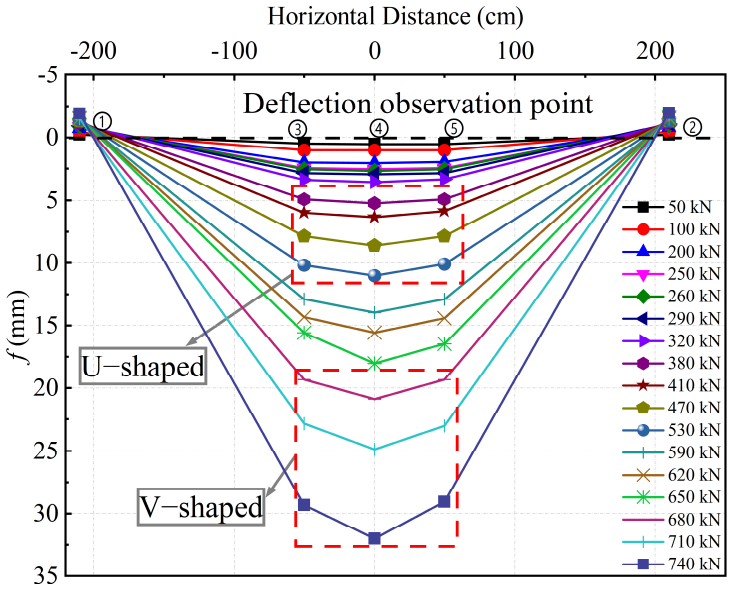


Figure 6. Pile deflection variation curve. (Among them, ①, ②, ③, ④, and ⑤ represent the location of the displacement sensor).

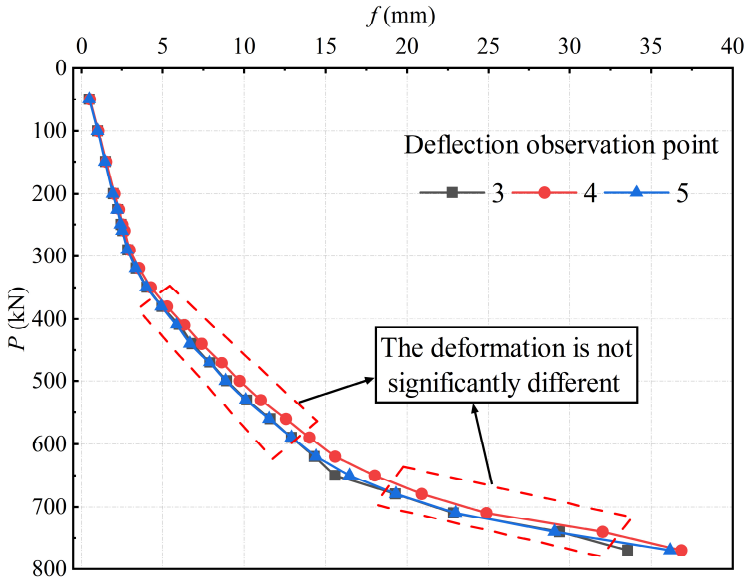


Figure 7. Deflection variation curve of mid span pure bending section.

3.3. Crack Distribution

Figure 8 shows the crack distribution of the PHSC500 (340) specimen. The first vertical crack appeared when the load reached 260 kN. When the load increased to 350 kN, the crack width near the midspan developed to 1.0 mm. As the load continued to increase, the internal stresses in the concrete were redistributed. The vertical cracks that formed at the edge of the tensile zone in the flexural–shear region gradually propagated diagonally and developed into inclined cracks. Eventually, a continuous and relatively wide critical diagonal crack was formed. At failure, the cracks were mainly distributed between the two supports. Vertical cracks were concentrated below the loading points and were relatively uniformly spaced, with a small number of cracks showing vertical branching. Inclined cracks were mainly located between the loading points and the supports. The total number of recorded independent cracks on the front and back surfaces was 166.



(**a**) (**b**)

Figure 8. Distribution of cracks in the test piece: (**a**) Appearance of the first crack; (**b**) Overall distribution of cracks.

3.4. Strain Distribution

Figure 9 shows the development of concrete strain with increasing load on the front section of the PHSC500 (340) specimen, where ε denotes strain. Before cracking, the strains at all measuring points were relatively small and increased approximately linearly with the load, which was generally consistent with the plane-section assumption. After cracking, the concrete strain in the tensile zone increased rapidly, causing some strain gauges to fail prematurely. Although several gauges continued to record data, their strain changes became slow or nearly stagnant. In contrast, a few gauges affected directly by cracks showed abrupt increases in strain, and their readings were no longer reliable. According to the test records, four strain gauges failed or produced abnormal readings during loading. These gauges were mainly located in the tensile zone and in regions where cracks were concentrated. The data recorded after gauge failure were not used for quantitative analysis of the sectional strain. Instead, they were used only as auxiliary evidence to identify crack development and the location of local damage. The strain in the compression zone increased steadily and was less affected by vertical cracking. As the load continued to increase, the cracks in the pile gradually widened and extended, and the neutral axis shifted upward. At the failure load, nearly all measured concrete strains approached 0.002.

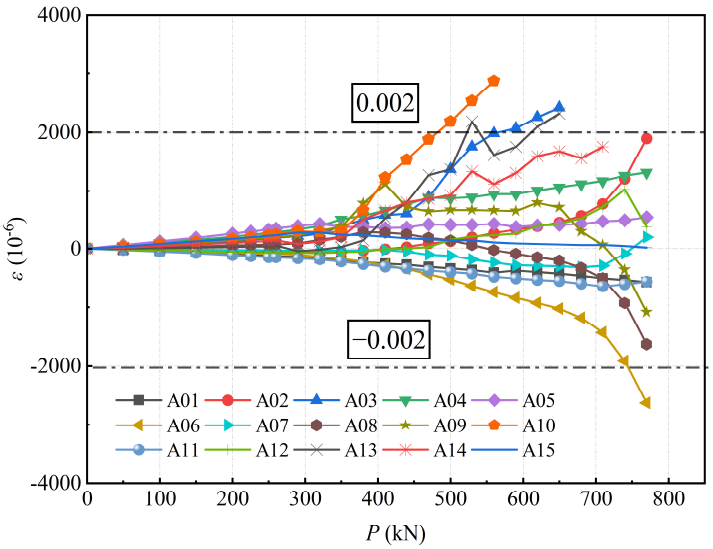


Figure 9. Concrete strain on the front face of the specimen.

Figure 10 shows the variation in concrete strain with load at the upper and lower surfaces of the midspan section. Compared with the strain development along the pile section, the strain at the midspan section developed more slowly and had a smaller mag-

nitude. In the early loading stage, the strain increased steadily. As the load approached the failure load, the strain increased sharply, and the maximum compressive strain at the upper surface reached 0.00217.

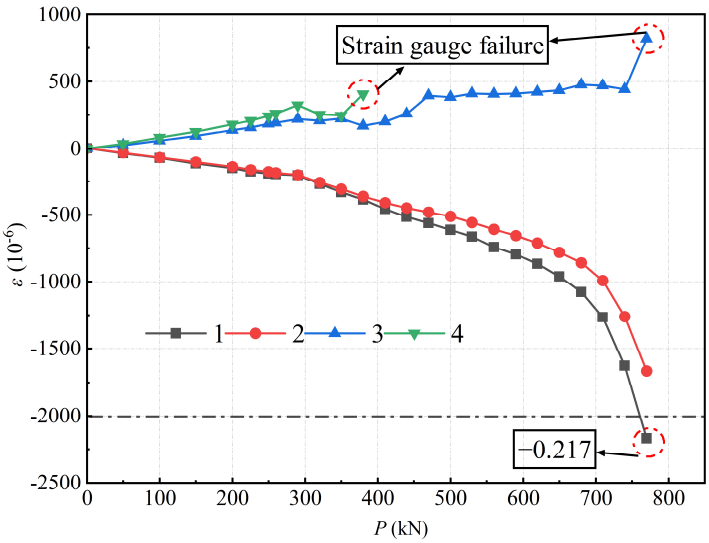


Figure 10. Concrete strain at the upper and lower surfaces of the midspan section.

4. Numerical Simulation

4.1. Model and Parameters

The finite element model of the PHSC pile is shown in Figure 11. To prevent stress concentration or numerical anomalies during loading, linear elastic steel bearing pads were placed at the supports and loading surfaces. Tie constraints were assigned between the steel pads and concrete, as well as between the end plates and concrete, to prevent separation during loading. The concrete and steel pads were modeled using three-dimensional solid elements C3D8R, whereas the reinforcement was modeled using two-node truss elements T3D2 and fully embedded in the concrete specimen. Prestress was applied using the equivalent cooling method. Specifically, the equivalent temperature drop was determined from the total prestress in the prestressing steel bars, the steel-bar area, the elastic modulus, and the coefficient of thermal expansion. This procedure introduced the initial tensile stress into the prestressing steel bars.

The mesh size was determined by considering the structural geometry, stress-gradient distribution, and computational efficiency. For mesh generation, the pile cross-section was divided into 10 equal segments along the side length, and the hollow region was divided into 24 segments. The element length was set to 50 mm in the pure bending region at midspan and near the loading points, whereas a mesh size of 100 mm was used in the remaining regions. In the finite element model, the concrete of the pile was simulated using the concrete damage plasticity (CDP) model. This model combines isotropic damage elasticity with tensile and compressive plasticity theories and can describe nonlinear concrete behavior, including tensile cracking and compressive damage. The CDP plasticity parameters used in this study were mainly determined with reference to the ABAQUS CDP parameter calibration method proposed by Liu et al. [38] and the finite element modeling approach for reinforced concrete members reported by Genikomsou and Polak [39]. The tensile and compressive damage parameters of concrete were determined based on the measured material properties of C80 concrete and the corresponding stress–strain relationships. The material parameters of the pile concrete and reinforcement are listed in Tables 3 and 4, respectively.

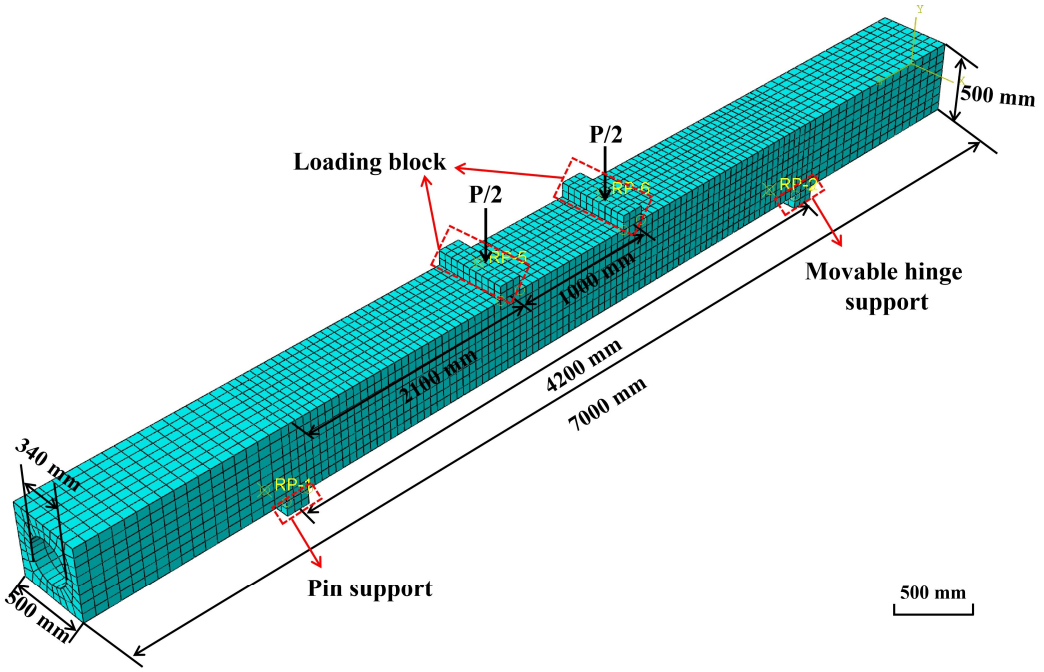


Figure 11. Schematic diagram of finite element model.

Table 3. Physical parameters of pile model.

ρ (kg·m^{-3})	E (MPa)	v	μ	K	ψ (°)	e	F_{b0}/F_{c0}
2300	38,000	0.2	0.0005	0.667	30	0.1	1.16

Note: ρ = Density; E = Elastic modulus; v = Poisson's ratio; μ = Viscosity parameter; K = Shape factor; ψ = Expansion angle; e = Eccentricity; F_{b0}/F_{c0} = Concrete biaxial compressive strength/Uniaxial compressive strength of concrete.

Table 4. Physical and mechanical parameters of reinforcement.

Reinforcement Type	ρ (kg·m^{-3})	E (MPa)	v	Coefficient of Thermal Expansion (°C^{-1})
Prestressing steel bars	7850	190,000	0.3	1.2×10^{-5}
Non-prestressed reinforcement	7850	200,000	0.3	
Stirrups	7850	200,000	0.3	

4.2. Model Validation

ABAQUS was used to perform a finite element back-analysis of the laboratory flexural test to verify the reliability of the model in predicting the flexural performance of the pile. Figure 12 compares the load–midspan deflection curves of the PHSC500 (340) specimen obtained from the test and the finite element analysis. The ultimate flexural capacity calculated by the finite element model differed from the experimental value by 4.23%, which was within 10%. The numerical curve also showed good agreement with the experimental curve. At the initial loading stage, the finite element curve was generally consistent with the experimental curve. This indicates that the initial stiffness of the model and the method used to introduce prestress were generally reasonable. As the load increased, the finite element curve shifted to the right earlier than the experimental curve, indicating an earlier reduction in stiffness. This difference was mainly associated with the smeared treatment of concrete cracking and damage in the CDP model.

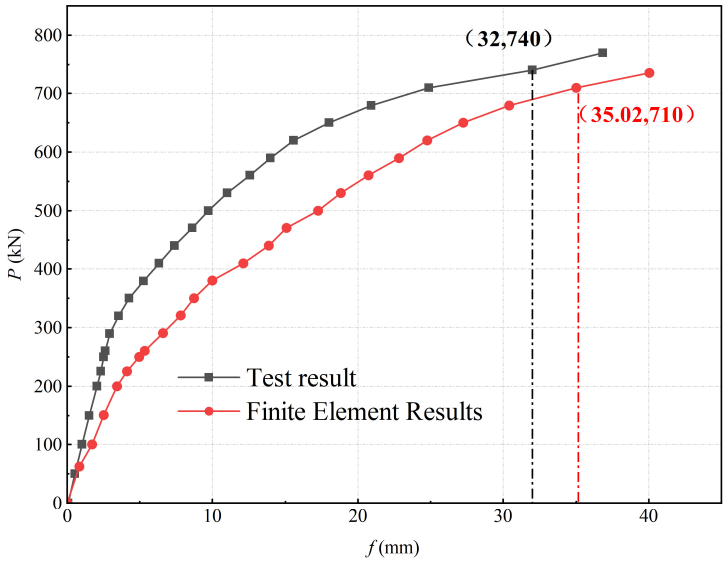
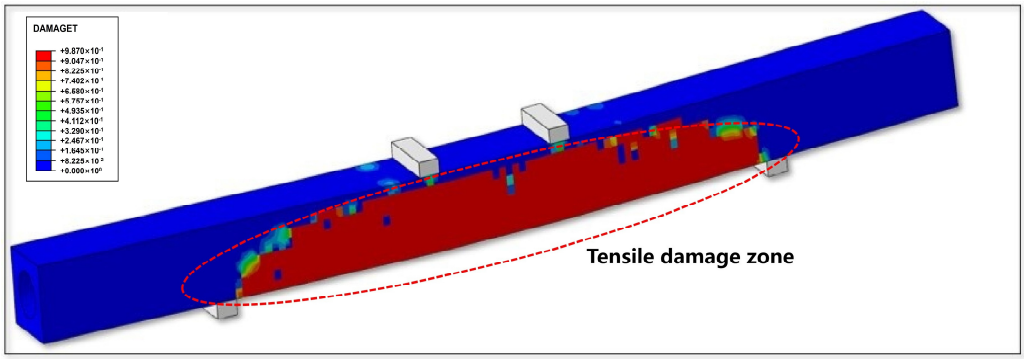


Figure 12. Comparison diagram of load–midspan deflection curve of hollow square pile.

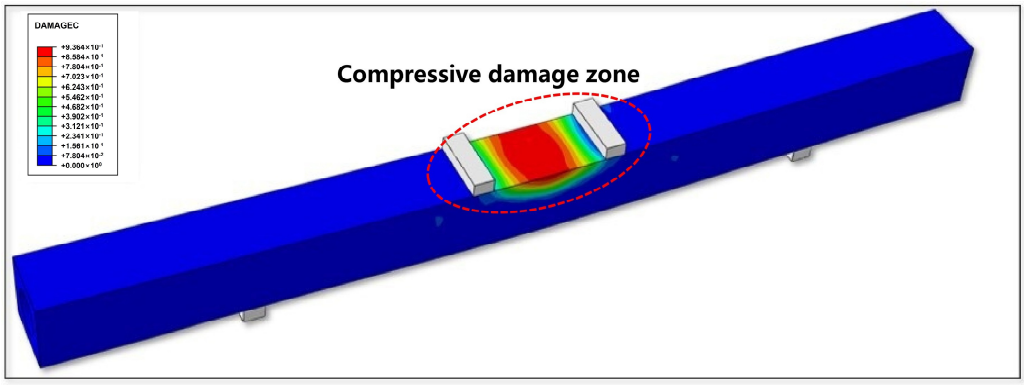
The failure modes obtained from the experiment and numerical simulation were further compared. Figure 13 shows the contour plots of concrete tensile damage, compressive damage, and maximum principal tensile stress at the ultimate state. The tensile and compressive damage variables are scalar damage indices ranging from 0 to 1. A value of 0 indicates that the corresponding type of damage has not occurred, whereas a value closer to 1 indicates more severe stiffness degradation under the corresponding stress state. A tensile damage variable approaching 1 indicates that tensile cracking of concrete has fully developed in that region and that the tensile stiffness has been substantially reduced. A compressive damage variable approaching 1 indicates severe compressive damage or a tendency toward local crushing. However, it does not correspond to element deletion in the finite element model or complete macroscopic fracture. As shown in the figure, a large tensile damage zone developed in the tensile region of the pile at the later loading stage. The tensile damage value approached 1, indicating that the concrete in the tensile region had fully cracked and no longer contributed effectively to tensile resistance. The tensile force was therefore mainly carried by the reinforcement. Meanwhile, the maximum principal tensile stress was mainly concentrated near the loading points and in the tensile region of the flexural–shear zone. Its distribution was generally consistent with the tensile damage concentration zones. This indicates that these regions were the primary locations for preferential crack development and were in good agreement with the positions of the critical diagonal cracks observed in the test. A distinct compressive damage zone appeared in the compression region of the flexural–shear zone. The damage propagated from the interior toward the exterior, showing clear crushing characteristics. By combining the tensile damage, maximum principal tensile stress distribution, and compressive damage characteristics, it can be inferred that the structure first experienced tensile cracking under flexural action. Subsequently, concrete in the compression region of the flexural–shear zone was progressively crushed, eventually leading to a shear–compression failure mode.

Because the concrete was modeled using the concrete damage plasticity model, which adopts a continuum damage formulation, the numerical simulation could not reproduce a failure pattern completely identical to that observed in the test. Nevertheless, the simulated damage zones and their development trends were generally consistent with the experimentally observed diagonal crack locations and shear–compression failure characteristics. Based on the comparison of the load–deflection curve and ultimate load-bearing capacity, the finite element model adopted in this study can reasonably reproduce the main flexural

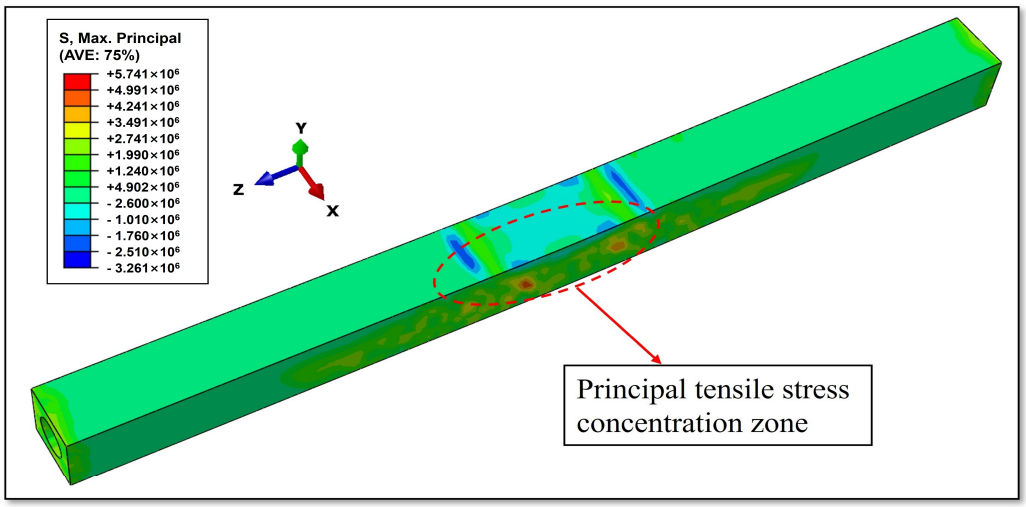
response and shear–compression failure characteristics of PHSC piles under the specimen geometry, material properties, reinforcement layout, prestress level, and loading conditions considered herein. Therefore, this model can provide a reasonable basis for subsequent comparative parametric analyses of the flexural performance of different pile types and reinforcement-ratio combinations. It should be noted that the subsequent numerical analyses are mainly intended to reveal the relative effects of section geometry, prestressing reinforcement ratio, and non-prestressed reinforcement ratio on flexural capacity, stiffness degradation, and ductility under the same modeling assumptions, boundary conditions, and loading mode. The conclusions therefore mainly reflect the variation trends within the parameter range selected in this study.



(**a**)



(**b**)



(**c**)

Figure 13. Distribution of tensile and compressive damage in concrete: (**a**) Tensile damage; (**b**) Compressive damage; (**c**) Maximum principal tensile stress distribution.

4.3. Case Configuration

After the accuracy of the model was validated, finite element models of different pile types were established under the same displacement-controlled loading condition to investigate their flexural performance. The analyzed pile types included the PHSC500 (340) pile, denoted as PHSC1-1; the composite-reinforced prestressed concrete pipe pile PRC500 (125), denoted as PRC1; and the composite-reinforced prestressed concrete hollow rectangular pile PHSC600 × 320 (200), denoted as PHSC3. To further evaluate the influence of different reinforcement configurations on the flexural performance of PHSC piles, several finite element models with varying reinforcement ratios were developed. The detailed parameters of each model are listed in Table 5.

Table 5. Finite element model and parameters for bending resistance.

Model No.	*B* (*D*) (mm)	Prestressing Steel	HRB400 Reinforcement	Stirrups	Prestressing Reinforcement Ratio (%)	HRB400 Reinforcement Ratio (%)	Total Reinforcement Ratio (%)
PHSC1-1	500 (340)	$12A^{D}12.6$	6C18	$A^{b}5@45/80$	0.94	0.96	1.90
PRC1	500 (125)	$12A^{D}12.6$	12C12	$A^{b}5@45/80$	1.02	0.92	1.94
PHSC3	600 × 320 (200)	$12A^{D}12.6$	2C12	$A^{b}5@45/80$	0.87	0.26	1.13
PHSC1-2	500 (340)	$12A^{D}12.6$	6C12	$A^{b}5@45/80$	0.94	0.76	1.70
PHSC1-3	500 (340)	$12A^{D}12.6$	6C16	$A^{b}5@45/80$	0.94	0.43	1.37
PHSC2-1	500 (340)	$12A^{D}10.7$	6C18	$A^{b}5@45/80$	0.78	0.96	1.74
PHSC2-2	500 (340)	$12A^{D}10.7$	6C18	$A^{b}5@45/80$	0.78	0.76	1.54
PHSC2-3	500 (340)	$12A^{D}10.7$	6C18	$A^{b}5@45/80$	0.78	0.43	1.21
PHSC3-1	500 (340)	$12A^{D}9.0$	6C18	$A^{b}5@45/80$	0.48	0.96	1.44
PHSC3-2	500 (340)	$12A^{D}9.0$	6C18	$A^{b}5@45/80$	0.48	0.76	1.24
PHSC3-3	500 (340)	$12A^{D}9.0$	6C18	$A^{b}5@45/80$	0.48	0.43	0.91

4.4. Flexural Performance Comparison

4.4.1. Effect of Pile Type on Flexural Performance

The load–midspan deflection curves of different pile types are shown in Figure 14. The cracking load of the PHSC1-1 specimen was 38.46% and 54.23% higher than those of the PRC1 and PHSC3 specimens, respectively. Its ultimate flexural capacity was also substantially higher than those of the PRC1 and PHSC3 specimens. To clarify the fundamental differences in flexural performance among the different pile types, the results were analyzed from several aspects.

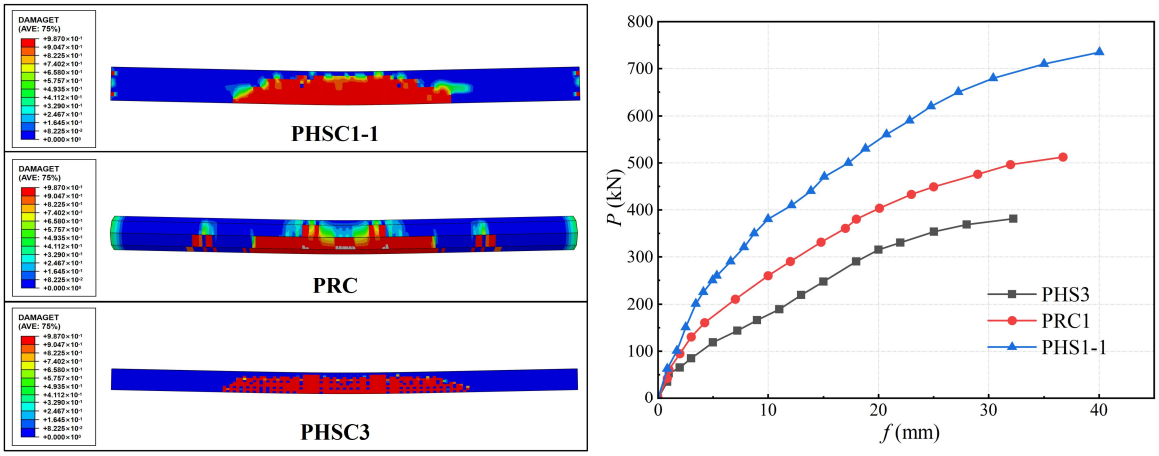


Figure 14. Comparison of load–midspan deflection curves of different pile types.

The section depth of PHSC1-1 was 500 mm, whereas the effective depth of PHSC3 was only 320 mm. Although PHSC3 had a larger section width, its overall flexural capacity remained lower than that of PHSC1-1 because flexural performance is more sensitive to

section depth. PRC1 had the same outer diameter as PHSC1-1; however, it had a circular hollow section. The material distribution relative to the neutral axis was less favorable than that of the square section, which also resulted in lower flexural performance than PHSC1-1.

The area of ordinary reinforcement in the tensile zone of PHSC1-1 was 6C18, which was larger than the 2C12 reinforcement used in PHSC3. This contributed to the improved flexural capacity of PHSC1-1. Although the ordinary reinforcement area of PRC1 reached 2C12, the reinforcement was distributed circumferentially, leading to a lower effective utilization ratio in the tensile zone and a limited contribution to flexural resistance.

Under the composite reinforcement system, the tensile reinforcement in PHSC1-1 could be more fully mobilized. In contrast, the non-prestressed reinforcement ratio of PHSC3 was only 0.26%, and the tensile force was mainly carried by the prestressing steel bars. This led to reductions in both the cracking load and ultimate load-bearing capacity. Although the reinforcement ratio of PRC1 was close to that of PHSC1-1, its circular hollow section and circumferential reinforcement arrangement reduced the efficiency of force resistance. Therefore, its flexural performance remained relatively weak. Overall, the differences in flexural performance among the pile types were mainly governed by section dimensions, the area of ordinary reinforcement in the tensile zone, and the reinforcement ratio.

4.4.2. Effect of Reinforcement Ratio on Flexural Performance

To investigate the effect of reinforcement ratio on the flexural performance of PHSC piles, the load–midspan deflection curves obtained from the numerical simulations were analyzed. The ductility coefficient was also adopted as an evaluation index to assess the flexural behavior of the specimens with different reinforcement configurations. The ductility coefficient was calculated as follows:

$$\mathrm{DI} = \Delta u / \Delta y \tag{2}$$

where Δu is the deflection corresponding to the ultimate load, and Δy is the yield deflection. Because PHSC piles contain both prestressing steel bars and non-prestressed reinforcement, the overall yield point of the member during flexural loading is difficult to determine directly. If the first yielding of ordinary reinforcement is used as the yield point, the transition of the overall member stiffness from the elastic stage to the nonlinear stage cannot be fully captured. Therefore, based on existing ductility evaluation methods for concrete members and relevant studies [40,41], the deflection corresponding to $0.75P_{\mathrm{u}}$ was adopted as the yield deflection in this study. This definition was mainly used to compare the relative ductility trends under different reinforcement-ratio conditions. Compared with the bilinear method or the first-yield method of reinforcement, this approach may lead to differences in the calculated ductility coefficient. If the deflection corresponding to $0.75P_{\mathrm{u}}$ is larger than the actual yield deflection, the calculated ductility coefficient may be underestimated. Conversely, it may be overestimated. Because the same definition was adopted for all cases, this difference does not affect the relative comparison among different reinforcement-ratio conditions. Similar methods have been used in some ductility studies on reinforced concrete and prestressed concrete members and are applicable for relative ductility comparisons among similar members with different parameter conditions.

As shown in Figure 15, the load–midspan deflection curves of the PHSC piles differed markedly under different reinforcement ratios. Table 6 presents the calculated ductility coefficients for each case. Overall, both the cracking load and the ultimate flexural capacity increased significantly with increasing reinforcement ratio. When the prestressing reinforcement ratio was kept at 0.94%, the cracking load of the specimen with a non-prestressed reinforcement ratio of 0.96% was approximately 29.79% and 38.46% higher than those of the specimens with non-prestressed reinforcement ratios of 0.76% and 0.43%, respectively. Its

ultimate flexural capacity was 1.17 and 1.48 times those of the latter two specimens, respectively. When the prestressing reinforcement ratio was 0.78%, the cracking load increased by 11.27% and 24.18% compared with the specimens with non-prestressed reinforcement ratios of 0.76% and 0.43%, respectively. The corresponding ultimate flexural capacities were 1.12 and 1.17 times those of the two specimens. When the prestressing reinforcement ratio was 0.48%, both the cracking load and the ultimate flexural capacity were lower than those of the specimens with prestressing reinforcement ratios of 0.78% and 0.94%. This indicates that a relatively low prestressing level has a limited effect on improving cracking resistance and load-bearing capacity.

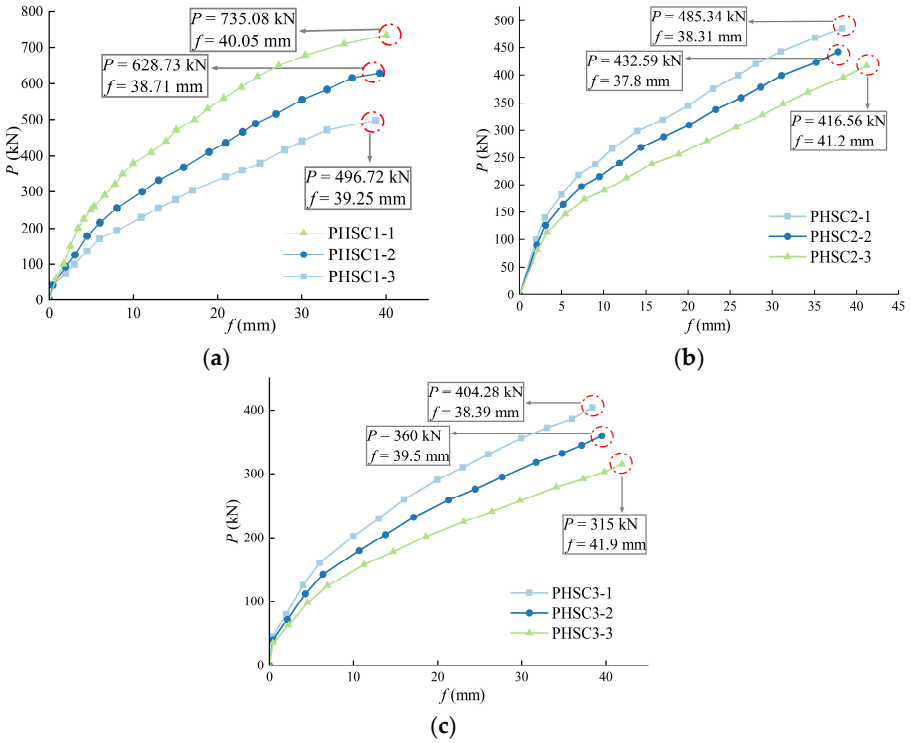


Figure 15. Load–midspan deflection curves under different reinforcement ratios: (**a**) Prestressing reinforcement ratio of 0.94%; (**b**) Prestressing reinforcement ratio of 0.78%; (**c**) Prestressing reinforcement ratio of 0.48%.

Table 6. Ductility coefficient of PHSC piles under different reinforcement ratios.

Prestressed Rebar Ratio (%)	Non-Prestressed Rebar Ratio (%)	P_u (kN)	Δ*y* (mm)	Δ*u* (mm)	DI
0.48	0.96	404.28	23	38.39	1.67
0.48	0.76	360	24.4	39.5	1.62
0.48	0.43	315	26.3	41.9	1.59
0.78	0.96	485.34	22	38.31	1.74
0.78	0.76	432.59	21.8	37.8	1.73
0.78	0.43	416.56	24.3	41.2	1.7
0.94	0.96	735.08	19.8	40.05	2.02
0.94	0.76	496.72	23.1	38.79	1.68
0.94	0.43	628.73	25.4	39.25	1.55

As shown in Table 6, when the prestressing reinforcement ratio increased from 0.48% to 0.78%, the ductility coefficient generally increased. This indicates that increasing the prestressing reinforcement ratio can improve the post-cracking deformation capacity and overall ductility of the member. However, when the prestressing reinforcement ratio further increased to 0.94%, the ductility coefficient showed noticeable fluctuations. This suggests

that an excessively high prestressing level may restrain post-cracking deformation development when the amount of ordinary reinforcement is insufficient, thereby weakening the improvement in ductility. Under the same prestressing reinforcement ratio, the ductility coefficient decreased as the non-prestressed reinforcement ratio decreased from 0.96% to 0.43%. This indicates that non-prestressed reinforcement plays an important role in deformation compatibility and ductility development after cracking. When the non-prestressed reinforcement ratio is low, crack propagation accelerates, the sectional deformation capacity decreases, and the ductility is consequently reduced. Comparison of the flexural capacity and ductility under different reinforcement ratios shows that increasing the prestressing reinforcement ratio can significantly improve the flexural capacity of the specimen. However, ductility does not increase monotonically with the prestressing reinforcement ratio.

Based on the variations in load-bearing capacity and ductility under different reinforcement ratios, the prestressing steel bars mainly improve the cracking load and ultimate load-bearing capacity of PHSC piles. In contrast, the non-prestressed reinforcement mainly improves post-cracking deformation compatibility and ductility. The finite element results show that the load-bearing capacity generally increases with increasing prestressing reinforcement ratio, whereas the ductility index does not increase monotonically. When the prestressing reinforcement ratio was 0.78%, the member exhibited a relatively balanced performance in terms of load-bearing capacity and ductility. Under the same prestressing reinforcement ratio, the ductility changed only slightly when the non-prestressed reinforcement ratio decreased from 0.96% to 0.76%. However, when it further decreased to 0.43%, the ductility coefficient showed a decreasing trend. This indicates that insufficient non-prestressed reinforcement may weaken the post-cracking deformation capacity of the member. It should be noted that each reinforcement-ratio case in this study was analyzed based on a single numerical simulation. Repeated simulations were not performed, and confidence intervals were not provided. Therefore, these results mainly reflect the relative variation trends within the selected parameter range of this study. The reinforcement design of PHSC piles should not focus solely on increasing the prestressing reinforcement ratio. The contribution of non-prestressed reinforcement to post-cracking deformation and ductility retention should also be considered.

5. Conclusions

In this study, a four-point bending test was conducted on a full-scale PHSC500 (340) hollow square pile specimen to investigate its flexural performance. A finite element model was also established to compare different pile types and reinforcement-ratio configurations. The main conclusions are as follows:

(1) At the initial loading stage, the load–midspan deflection response of the PHSC500 (340) specimen was approximately linear. As the load increased, the internal stresses in the concrete were redistributed. The number of vertical cracks increased, and their propagation directions changed. A critical diagonal crack eventually formed at the edge of the tensile zone in the flexural–shear region, and the specimen ultimately exhibited a shear–compression failure mode.

(2) Before cracking, the initial tensile stress in the prestressing steel bars restrained deformation in the tensile zone. As a result, the overall pile deflection was small and increased gradually, showing a U-shaped deflection profile. The strains at the measuring points of each section were also relatively small, which was generally consistent with the plane-section assumption. At the failure stage, the concrete strain approached 0.002. Meanwhile, the midspan deflection increased rapidly, the deformation rate of the pile accelerated markedly, and the deflection curve changed to a V-shaped profile.

(3) The ABAQUS finite element model reasonably simulated the load–midspan deflection response and damage development of the PHSC500 (340) hollow square pile under flexural loading. The ultimate bending moment calculated by the model differed from the experimental result by 4.23%, and the numerical curve was generally consistent with the test curve. The tensile and compressive damage zones were mainly concentrated in the tensile zone and the compression zone of the flexural–shear region, respectively. These distributions were consistent with the experimentally observed diagonal crack propagation and shear–compression failure characteristics, indicating that the finite element model can reasonably reproduce the main flexural response and failure characteristics of the tested PHSC pile under the geometry and loading conditions considered in this study.

(4) Under the same modeling and loading conditions, the cracking load and ultimate flexural capacity of the PHSC1-1 pile were greater than those of the PRC1 and PHSC3 piles. This indicates that section geometry and reinforcement configuration significantly affect the load-bearing performance of the member. The results for different reinforcement ratios show that prestressing steel bars mainly improve the cracking load and ultimate load-bearing capacity, whereas non-prestressed reinforcement mainly improves post-cracking deformation compatibility and ductility. However, the ductility index did not increase monotonically with the prestressing reinforcement ratio. Within the parameter range considered in this study, the member showed a relatively balanced performance in terms of load-bearing capacity and ductility when the prestressing reinforcement ratio was approximately 0.78%. When the non-prestressed reinforcement ratio was too low, the post-cracking deformation capacity decreased markedly. However, this result was mainly obtained from finite element parametric analysis. Before it is used in engineering design, it should be further validated using full-scale tests and actual engineering conditions. These results can provide a reference for the subsequent optimization of reinforcement parameters.

Author Contributions: Conceptualization, H.X. and Z.Z.; methodology, H.X. and Z.Z.; software, H.X. and Z.Z.; validation, H.X. and Z.Z.; formal analysis, H.X. and Z.Z.; investigation, H.X. and Z.Z.; writing—original draft preparation, H.X. and Z.Z.; writing—review and editing, H.X. and Z.Z.; supervision, H.X. and Z.Z. All authors have read and agreed to the published version of the manuscript.

Funding: This research was funded by the Shaanxi Provincial Transportation Department Project, grant number 23-72K.

Institutional Review Board Statement: Not applicable.

Informed Consent Statement: Not applicable.

Data Availability Statement: The data that support the findings of this study are available upon reasonable request from the corresponding author [Zhijun Zhou, zhouzhijun@chd.edu.cn]. The main experimental and numerical results are presented in the figures and tables of this manuscript.

Conflicts of Interest: The authors declare no conflicts of interest.

References

1. Akiyama, M.; Abe, S.; Aoki, N.; Suzuki, M. Flexural test of precast high-strength reinforced concrete pile prestressed with unbonded bars arranged at the center of the cross-section. *Eng. Struct.* **2012**, *34*, 259–270. [CrossRef]
2. Hou, Z.; Liu, Y.; Han, Z.; Tang, M.; Gong, X.; Su, D.; Wang, L. Experimental Study of the Bearing Characteristics of a Novel Energy-Saving and Environmentally Friendly Pile: Drilling with Prestressed Concrete Pipe Cased Piles. *Int. J. Geomech.* **2024**, *24*, 04024035. [CrossRef]

3. Xu, J.; Ma, L. Study on bearing capacity of prestressed pipe pile foundation under horizontal load. *Open Constr. Build. Technol. J.* **2017**, *11*, 301–312. [CrossRef]
4. Yang, Z.; Li, G.; Wang, W. Experimental investigation and nonlinear finite element analysis on seismic performance of PHC piles. *Struct. Eng. Int.* **2018**, *28*, 475–488. [CrossRef]
5. Yang, Z.; Wang, W. Experimental and Numerical Investigation on the Behaviour of Prestressed High Strength Concrete Pile-to-pile Cap Connections. *KSCE J. Civ. Eng.* **2016**, *20*, 1903–1912.
6. Liu, H.; Kong, G.; Ding, X.; Chen, Y. Performances of large-diameter cast-in-place concrete pipe piles and pile groups under lateral loads. *J. Perform. Constr. Facil.* **2013**, *27*, 191–202. [CrossRef]
7. Wang, H.; Gan, G.; Zeng, K.; Chen, K.; Yu, X. Study on Flexural Performance of Prestressed Concrete Steel Strand Square Piles with Reinforcement. *Buildings* **2022**, *12*, 1801. [CrossRef]
8. Wang, T.; Liu, H.; Kang, M.; Zhao, B.; Shen, J.; Li, Y.; Yang, Y. Study on the Synergistic Effect of Primary Support and Surrounding Rock of Large Buried Depth Tunnel in Soft and Fractured Strata. *Appl. Sci.* **2024**, *14*, 2028. [CrossRef]
9. Wu, P.; Guo, Y.; Zhu, D.; Jin, W.; Zhang, Z.; Liang, R. Flexural performances of prestressed high strength concrete piles reinforced with hybrid GFRP and steel bars. *Mar. Georesources Geotechnol.* **2020**, *38*, 518–526.
10. Yang, Y.; Xue, Y.; Yu, Y.; Ma, N.; Shao, Y. Experimental study on flexural performance of partially precast steel reinforced concrete beams. *J. Constr. Steel Res.* **2017**, *133*, 192–201. [CrossRef]
11. Guo, Y.; Wu, P.; Han, L.; Zhang, Z.; Han, Z. Experimental study and numerical analysis on bending capability of compositely reinforced (GFRP) prestressed concrete pipe pile. *Chin. J. Undergr. Space Eng.* **2019**, *15*, 481–488. (In Chinese)
12. Liu, Y.; Liu, Y.; Li, B.; Zhang, G.; Hu, Z.; Liu, J. Flexural tests and numerical simulations of prestressed concrete pipe piles with partial hybrid reinforcement based on support of foundation pits. *Chin. J. Geotech. Eng.* **2024**, *46*, 406–414. (In Chinese) [CrossRef]
13. Liu, H.; Wang, T.; Ma, W.; Kang, M.; Fu, Y.; Yan, T. Research on the Settlement Patterns of Tunnel-Surrounding Rock Under Groundwater Conditions. *Appl. Sci.* **2025**, *15*, 3796. [CrossRef]
14. Karayannis, C.G.; Chalioris, C.E. Strength of prestressed concrete beams in torsion. *Struct. Eng. Mech.* **2000**, *10*, 165–180. [CrossRef]
15. Zhang, W.; Zheng, D.; Huang, Y.; Kang, S. Experimental and simulative analysis of flexural performance in UHPC-RC hybrid beams. *Constr. Build. Mater.* **2024**, *436*, 136889. [CrossRef]
16. Thusoo, S.; Kono, S.; Hamada, J.; Asai, Y. Performance of precast hollow steel-encased high-strength concrete piles. *Eng. Struct.* **2020**, *204*, 109995. [CrossRef]
17. El-Helou, R.G.; Graybeal, B.A. Flexural behavior and design of ultrahigh-performance concrete beams. *J. Struct. Eng.* **2022**, *148*, 04022013. [CrossRef]
18. Hao, N.; Yang, Y.; Xue, Y.; Feng, S.; Yu, Y.; Wang, C.; Li, Y. Experimental study on flexural behavior of partially precast high-strength steel reinforced ultra-high performance concrete beam. *Eng. Struct.* **2023**, *284*, 115999.
19. Peng, F.; Deng, J.; Xue, W. Flexural behavior and design of ultrahigh-performance concrete beams reinforced with GFRP bars. *J. Compos. Constr.* **2024**, *28*, 04024019. [CrossRef]
20. Ren, J.; Xu, Q.; Chen, G.; Liu, C.; Gong, S.; Lu, Y. Flexural performance of pretensioned centrifugal spun concrete piles with combined steel strands and reinforcing bars. *Structures* **2021**, *34*, 4467–4485. [CrossRef]
21. Xu, Q.; Chen, G.; He, J.; Gong, S.; Xiao, Z. Flexural performance experiment of connection joint for composite reinforcement concrete prefabricated square piles. *J. Zhejiang Univ. (Eng. Sci.)* **2017**, *51*, 1300–1308. (In Chinese) [CrossRef]
22. Xu, Y.; Chen, Z.; Fan, J.; Li, Z.; Zhang, K.; Tu, X. Study on the Flexural Performance of Prestressed Concrete Solid Square Piles and Resilient Clamping Connections. *KSCE J. Civ. Eng.* **2023**, *27*, 285–298.
23. Sun, C.; Miao, C.; Li, A.; Xian, C.; Zhu, F. Experimental study on seismic performance of prestressed concrete solid pile using mechanical connection. *World Earthq. Eng.* **2019**, *35*, 39–49.
24. Gong, S.; Zhao, Y.; Fan, H.; Xu, S.; Xu, Q.; Ren, J.; Lu, Y. Experimental study on seismic performance of prestressed concrete solid square piles. *Adv. Struct. Eng.* **2024**, *27*, 2444–2462. [CrossRef]
25. Ji, Z.; Wu, J.; Wang, L.; Dong, G.; Tan, Z.; Zhao, J.; Wang, Y. Research on the flexural performance of recycled coarse aggregate concrete beams after carbonation. *J. Build. Eng.* **2024**, *97*, 110645. [CrossRef]
26. Bolina, F.; Henn, A. Eco-Friendly Reinforced Concrete Beams Exposed to Standardized Fire: A Thermal Finite Element Analysis. *Sustainability* **2025**, *17*, 2951. [CrossRef]
27. Liu, Y.; Wang, Q.; Zhu, M. Influence of effective stress on mechanical behaviors of prestressed pipe piles. *Chin. J. Geotech. Eng.* **2013**, *35*, 1130–1133. (In Chinese)
28. Sun, C.; Zhuang, M.; Gao, L.; Yan, J.; Yu, T.; Liu, T. Experimental Study on Seismic Performance Improvement of Pile-Cap Joints in a Prestressed Concrete Solid Square Pile Using a Snap-In Mechanical Connection. *J. Earthq. Eng.* **2023**, *27*, 3180–3201.
29. Su, Y.; Wu, C.; Shang, J.; Zhang, P.; Sheikh, S.A. Experimental and numerical simulation research on the flexural performance of beams reinforced with GFRP bars and three-sides UHPC layer. *Structures* **2024**, *59*, 105746.

30. Xu, Q.; Chen, G.; He, J.; Gong, S. Flexural performance experiment of composite reinforcement concrete prefabricated square piles. *Chin. J. Zhejiang Univ. (Eng. Sci.)* **2016**, *50*, 1768–1776. (In Chinese)
31. Xu, W.; Miao, H.; Chen, Y. Pull-out behavior and damage assessment of core concrete of full-scale prestressed high-strength hollow square piles. *Structures* **2023**, *51*, 1906–1918.
32. Sun, Q.; Yang, Y.; Fan, J.; Zhang, Y.; Bai, Y. Effect of longitudinal reinforcement and prestressing on stiffness of composite beams under hogging moments. *J. Constr. Steel Res.* **2014**, *100*, 1–11. [CrossRef]
33. *JGJ 19-2010*; Technical Specification for Application of Cold-Drawn Low-Carbon Steel Wire. China Architecture & Building Press: Beijing, China, 2010. (In Chinese)
34. *GB/T 13476-2023*; Pretensioned Spun Concrete Piles. China Standards Press: Beijing, China, 2023. (In Chinese)
35. *GB/T 50152-2012*; Standard for Test Method of Concrete Structures. China Architecture & Building Press: Beijing, China, 2012. (In Chinese)
36. *T/CECS 582-2019*; Technical Specification for Precast Concrete Sheet Pile Retaining Wall. China Planning Press: Beijing, China, 2019. (In Chinese)
37. *GB 50010-2010*; Code for Design of Concrete Structures. China Architecture & Building Press: Beijing, China, 2010. (In Chinese)
38. Liu, W.; Xu, M.; Chen, Z. Parameters calibration and verification of concrete damage plasticity model of ABAQUS. *Ind. Constr.* **2014**, *44*, 167–171+213. (In Chinese)
39. Genikomsou, A.S.; Polak, M.A. Finite element analysis of punching shear of concrete slabs using damaged plasticity model in ABAQUS. *Eng. Struct.* **2015**, *98*, 38–48. [CrossRef]
40. Guo, S. Flexural Behavior of Graded High-Performance Crumb Rubber Concrete Beams. Master's Thesis, Guangzhou University, Guangzhou, China, 2025. (In Chinese)
41. Lopes, A.V.; Lou, T.; Lopes, S.M.R. On the ductility of RC beam section: A revision and up to date of conclusions. *Eng. Struct.* **2025**, *322*, 119105.

Disclaimer/Publisher's Note: The statements, opinions and data contained in all publications are solely those of the individual author(s) and contributor(s) and not of MDPI and/or the editor(s). MDPI and/or the editor(s) disclaim responsibility for any injury to people or property resulting from any ideas, methods, instructions or products referred to in the content.